Ceria-supported catalysts for CO abatement in combustion exhaust gases

Andrea Lazzarini[a,b,*], Luciano Atzori[c,*], Matteo Signorile[d], Francesco Ferella[a,e], Maria Giorgia Cutrufello[b,c], Elisabetta Rombi[b,c], Marcello Crucianelli[a,b]

[a] *Department of Physical and Chemical Sciences, University of L'Aquila, Via Vetoio ("A.C. De Meis" building), 67100, L'Aquila - Italy.*

[b] *Consorzio Interuniversitario Nazionale per la Scienza e Tecnologia dei Materiali (INSTM), Via Giuseppe Giusti 9, 50121 Firenze, Italy.*

[c] *Department of Chemical and Geological Sciences, University of Cagliari, Monserrato University Complex, S.S. 554 bivio Sestu, 09042, Monserrato (CA) - Italy.*

[d] *Department of Chemistry, NIS and INSTM Reference Centre, University of Torino, Via G. Quarello 15/A, 10135, Torino - Italy.*

[e] *INFN Gran Sasso National Laboratories, Via G. Acitelli 22, 67100, Assergi (AQ) - Italy.*

[*] *Corresponding authors: andrea.lazzarini@univaq.it; luciano.atzori@unica.it*

Abstract: we present a series of Ni, Fe, and mixed NiFe-based catalysts, deposited onto ceria prepared with either soft templated (with CTAB) or hard templated (with SBA-15) syntheses. The prepared materials were thoroughly characterized with SEM, HRTEM, EDX, ICP-MS, PXRD, and N_2 adsorption techniques, to fully comprehend their nature. All catalysts were then tested for carbon monoxide oxidation reaction at different temperatures, aiming to reach operative conditions typical of industrial plants (350-400 °C, in the presence of competitive species such as CO_2 and H_2O in the feed). Advanced reaction tests highlighted outstanding materials (especially NiFe catalyst deposited onto hard-templated ceria), displaying catalytic performances able to compete with those typical of noble metal-based catalysts. Such catalysts were further investigated by means of Raman and CO@FT-IR spectroscopy, unraveling their surface properties, which make them excellent candidates for replacing more costly noble metal-based catalysts currently employed for such reaction.

Keywords: CO oxidation; active supports; nanostructured ceria; bi-metal catalysts; environmental pollution.

1. Introduction

Environmental pollution has been a hot topic since decades either within or outside the scientific community. However, the recent acceleration of climate change and the apparent unstoppable growth in environment contamination due to human activities, has directed a large part of scientific efforts to invert such trend. The fastest route in which pollutants diffuse around the Earth is through atmosphere: global air quality not only negatively influences wildlife and accelerate ice melting at the Poles [1], but also affects health quality in human communities. Indeed, most of atmospheric pollution is produced within metropolitan areas, where nowadays almost 57% of the total human population resides [2] and industrial activities are concentrated, meaning a tremendous risk for the inhabitants in those areas. Particulate, Polycyclic Aromatic Hydrocarbons (PAHs), as well as toxic gases (NO_x primarily) are the highest in concentration and among the most dangerous incomplete combustion byproducts. Nevertheless, while for these substances strict containment measures have already been implemented [3], there are still few compounds having lower restrictions compared to the previous ones. Among toxic gases, carbon monoxide (mainly produced through incomplete combustion of fossil fuels) is one of the most harmful gases for humans [4], due to its ability to interfere with oxygen coordination in hemoglobin. This phenomenon induces the production of carboxyhemoglobin [5-7], greatly affecting oxygen exchange even in low concentrations, potentially causing seizure, coma, and eventually death [8]. Therefore, controlling atmospheric CO level is of pivotal importance. Such problem has already been addressed concerning ground transportation of either people or goods. However, as far as the industrial activities are concerned, the matter was not tackled with the same determination. Nowadays, this issue is becoming more and more relevant, to the point that it has been regulated by European legislation regarding industrial and power plants [3]. One of the easiest ways to reduce atmospheric CO emissions is *via* oxidative processes, that is converting CO into CO_2, through the following reaction:

$$2\ CO + O_2 \rightleftarrows 2\ CO_2 \qquad \Delta_r H^\circ = -566\ kJ\ mol^{-1}$$

The current system employed for high temperature CO oxidation is a catalyst based on alumina honeycomb monolithic supports with platinum nanoparticles as active species [9-11]. Nonetheless, sometimes noble metal-based catalysts are over-performing for such reaction: indeed, they are often employed for hydrogen purification, in which CO oxidation takes place at much lower temperatures than the ones of combustion exhaust gases (<100 °C vs. 350-400 °C). Such systems involve mainly alumina-supported [12-17], titania-supported [18,19], and ceria-supported catalysts [20-28].

The turning point for such systems was the introduction of ceria among the oxides supporting the active phase of such catalysts [29]. Indeed, CeO_2 is able to withstand a cerium local reduction from Ce^{4+} to Ce^{3+}, by losing a coordinated oxygen atom that can then be employed in case of sub-stoichiometric oxidation conditions. The reversibility of the process allows the restoration of oxygen in the ceria structure whenever the catalyst is exposed to over-stoichiometric conditions. Therefore, ceria-supported catalysts are the best candidates for oxidation processes with fluctuating oxidant concentration [25], exploiting support properties in order to enhance the overall catalytic performances [17,30].

This phenomenon allows to move the focus for the active phase towards non-noble metals, which are still active at the operating temperature (above 350 °C) [31]. Among them, cobalt [32-36], iron [32,37-40], nickel [41-43], and their alloys [44-48] are the most investigated and promising systems to substitute noble metals in CO oxidation reaction. In particular, Ni belongs to the same group of Pt and Pd and possesses similar properties in terms of reactivity and possibilities concerning oxidative catalysis [42,49,50], although with a slightly lower activity. Nevertheless, it is way less expensive than noble metals and its performances can be strongly enhanced when alloys are formed, especially in the presence of iron, with which it is extremely soluble at almost any concentration [51-53]. Specifically, Fe-Ni alloy was successfully employed for CO oxidation in synergistic effect with platinum [44]. A well definite intermetallic species, namely $NiFe_3$ [53], was supported onto SiO_2 and fruitfully tested for olefins partial oxidation reactions in the liquid phase, providing excellent results [54].

Although reaction conditions for our target process are quite different, we strongly believe that a support exchange in favor of ceria might generate non-negligible benefits to the overall system when dedicated to gas phase CO oxidation. However, not all ceria structures might enhance catalytic results in the same manner: indeed, some crystal shapes might be more effective in promoting certain types of reactions [55]. Templating agents, either soft or hard, are currently employed to produce hierarchical [56] or porous structures [57-60], nanotubes [61], nanorods [62], and nanoparticles [26,63,64]. They can also be incorporated into mesoporous silica structures [65-70]. Yet, not all the above mentioned syntheses are easily performed, thus limiting their implementation for upscaling processes.

With all this in mind, we wanted to achieve the challenging target of producing an efficient, durable, and economically sustainable catalyst, able to compete at the same level with Pt ones in oxidizing carbon monoxide that is released in great amounts by industries and power plants. We started by selecting two ceria supports, by varying the aspect ratio of the crystals, with an eye on the ease of potential scalability of the process. Therefore, we selected soft-templated CeO_2 nanoparticles [50] and hard-templated CeO_2 nanorods [71], which are among the simplest and cheapest ceria nanomaterials to be produced. Afterwards, we deposited on both of them pure Fe and Ni phases, and a mixed one. We furthermore produced Pt-based catalysts, for the sake of comparison with non-noble metal catalyst. Differently from most of the literature on the topic [72-80], we decided to test our samples in conditions as close as possible to the operative ones, by taking into account not only catalytic performance in the sole presence of CO and O_2, but considering the overall composition of real combustion exhaust [81].

2. Experimental

2.1 Chemicals

Pluronic copolymer P123 ($EO_{20}PO_{70}EO_{20}$), tetraethyl orthosilicate 98 % (TEOS), hydrochloric acid 37 % (HCl), cerium(III) nitrate hexahydrate 98.5% ($Ce(NO_3)_3\ 6H_2O$), hexadecyltrimethylammonium

bromide 98% (CTAB), platinum(IV) chloride 96% ($PtCl_4$), nickel(II) acetate tetrahydrate ($Ni(OAc)_2$ $4H_2O$), anhydrous ethanol 99.5% (EtOH), and hydrogen peroxide 30%$_{v/v}$ (H_2O_2) were purchased by Sigma-Aldrich. Nitric acid 65% (HNO_3), sodium hydroxide 98% (NaOH), and potassium hydroxide 98% (KOH) were purchased by Carlo Erba reagents. Iron(II) chloride tetrahydrate 98% ($FeCl_2$ $4H_2O$) was purchased by Alfa Aesar. N_2 99.99%, Air 99.99%, CO_2 99.99%, and CO 5.01 % (in He) were purchased by Air Liquid. Liquid nitrogen ($N_{2(liq)}$), and CO 99.99% were purchased by Nippon gases. H_2O milliQ (resistivity 18.2 MΩ cm^{-1} at 25 °C) was obtained with a Merck-Millipore purification system. All chemicals were employed with no further purification.

2.2 Ceria soft-template synthesis

The preparation procedure for this support (CeO_{2_st} onwards) was adapted from ref. [50]. Briefly: inside a 1 L round-bottom flask, 21.7 g of $Ce(NO_3)_3$ $6H_2O$ and 150 mL of milliQ water were added and kept under vigorous stirring until the solution became crystal clear. Then, additional 100 mL of milliQ water and 11 g of CTAB as templating agent were added while stirring; immediately after this step the solution increased its viscosity. Afterwards, pH was adjusted to 12 by means of a 2 M KOH solution, turning to a light violet color. The obtained suspension was kept under stirring at 80 °C for 24 h. Then, reaction slurry was transferred inside centrifuge tubes and centrifuged at 5000 rpm for 20 min. The obtained solid was recovered, washed with milliQ water, and centrifuged at 5000 rpm for 20 min until the washing solution turned to a neutral pH. After that, the sample was dried in air at 80 °C overnight. Finally, the obtained nanoparticles were calcined in air at 600 °C for 10 h (T_{ramp} = 1 °C min^{-1}) to remove the templating agent.

2.3 Ceria hard-template synthesis

The preparation procedure for this support (CeO_{2_ht} onwards) was adapted from ref. [71]. Briefly: 7.6 g of $Ce(NO_3)_3$ $6H_2O$ were dissolved in 25 mL of EtOH. Afterwards, 1 g of SBA-15 silica as

templating agent (prepared according to literature procedure [82]) and 15 mL of the previously prepared $Ce(NO_3)_3$/EtOH solution were added in a 50 mL round-bottom flask and vigorously stirred for 3 h, in order to allow the diffusion of Ce cations inside the mesoporous silica channels. The suspension was then transferred inside a oven, where it was dried in air at 60 °C overnight. The recovered powder was reunited with the remaining 10 mL $Ce(NO_3)_3$/EtOH solution, vigorously stirred for 3 h, and dried overnight in air at 60 °C. The recovered powder was calcined in air at 600 °C for 10 h (T_{ramp} = 1 °C min^{-1}), allowing the formation of cerium oxide. In order to remove the templating agent, the sample was transferred inside a Teflon beaker with 20 mL of 2 M NaOH solution and heated at 50 °C for 2 h, enough to attack and remove completely the templating agent. The slurry was centrifuged at 5000 rpm for 20 min. The obtained solid was recovered, washed with milliQ water, and centrifuged at 5000 rpm for 20 min until the washing solution turned to a neutral pH. After that, the sample was dried in air at 80 °C overnight. Finally, the material was re-calcined in air at 500 °C for 10 h (T_{ramp} = 1 °C min^{-1}).

2.4 Single metal deposition

The single-metal catalysts were prepared by incipient wetness impregnation technique [18,83,84], aiming to a theoretical 5 $\%_{mol}$ metal loading over both CeO_{2_st} and CeO_{2_ht} supports. 500 mg of support and a proper amount of metal salt (alternatively $FeCl_2$ $4H_2O$, $Ni(OAc)_2$ $4H_2O$, or $PtCl_4$) were dissolved through ultrasound radiation and kept under vigorous stirring in air, for 5 h at room temperature, inside a 25 mL round-bottom flask. Afterwards, the slurry was transferred inside a crucible and dried in air overnight at 80 °C. Finally, the obtained powder was calcined in air at 600 °C for 3 h (T_{ramp} = 3 °C min^{-1}). Six samples were obtained and named according to the desired support and metal precursors as Fe/CeO_{2_st}, Ni/CeO_{2_st}, Pt/CeO_{2_st}, Fe/CeO_{2_ht}, Ni/CeO_{2_ht}, and Pt/CeO_{2_ht}.

2.5 Double metal deposition

The double-metal catalysts were synthesized through a preparation method adapted from ref. [54]. For this procedure, the selected Fe:Ni ratio was 1:3, still aiming to total active metal loading of a

theoretical 5 $\%_{mol}$. Briefly: 300 mg of support were placed inside a 50 mL round-bottom flask and suspended through ultrasound radiation in 10 mL of milliQ water. Then, 16.3 mg of $Ni(OAc)_2$ $4H_2O$ and 4.5 mg of $FeCl_2$ $4H_2O$ were added to the suspension and kept under stirring in air for 5 h at room temperature. Afterwards, the slurry was transferred inside a crucible and dried in air overnight at 80 °C. Finally, the obtained powder was calcined in air at 600 °C for 3 h (T_{ramp} = 3 °C min^{-1}). Two samples were obtained and named according to the desired support as $NiFe/CeO_{2\_st}$ and $NiFe/CeO_{2\_ht}$.

2.6 Characterization techniques

2.6.1 Electron Microscopy

Scanning Electron Microscopy (SEM) measurements were performed by means of a FESEM ZEISS Gemini 500 instrument, operating with an accelerating voltage of 20 kV. The samples were ground inside an agate mortar and powders were deposited directly onto a carbon-tape-covered stab.

Transmission Electron Microscopy (TEM) images and Scanning-Transmission elemental analyses (STEM-EDX) were obtained using a JEOL JEM 1400 Plus instrument operating at 120 kV, equipped with an Oxford Aztec spectrometer.

A JEOL JEM 2010 UHR microscope, operating at 200 kV and equipped with a Gatan Imaging Filter (GIF) with a 15 eV window and a 794 slow scan CCD camera, was instead used to collect High-Resolution Transmission Electron Microscopy (HRTEM) images. For both TEM and HRTEM techniques, finely ground samples were dispersed in n-octane in an ultrasonic bath. The suspension was then dropped on a copper grid covered with a carbon thin film for the observation.

2.6.2 Inductively Coupled Plasma-Mass Spectrometry (ICP-MS)

ICP-MS analyses were performed with a mass spectrometer Agilent 7850 with quadrupole analyzer, equipped with SPS 4 autosampler from Agilent. A 180 s wash-up with 2% HNO_3 was performed after each measurement, in order to eliminate any memory effect. All analyses were performed inside an ISO-6 clean room, thus reducing the risk of possible environmental contamination. Sample dissolution procedure was based on a literature procedure [85]. 5 mg of each sample was weighted in

previously conditioned PFA vials. Then, 1 mL of concentrated HNO_3 and 1 mL of H_2O_2 30%$_{v/v}$ were added to the vials and irradiated with ultrasound at 60 °C for 30 min, followed by a treatment at 120 °C for 1 hour. Afterwards, the samples were treated with 8 mL of milliQ water at 100 °C for 1 hour, followed by centrifugation to separate solid and supernatant. The remaining solid fraction was subjected to a second attack using 1 mL of concentrated HNO_3 at 120 °C for 1 hour, and then at 100 °C for 1 hour after 5 mL of milliQ water addition. Finally, the solutions obtained from the two attacks were reunited and diluted 1:50 for the ICP-MS analysis.

2.6.3 X-Ray Diffraction (XRD)

Structural features of the fresh and used samples were examined by XRD using a PANalyitical X'Pert PRO diffractometer with a Cu Kα radiation, a secondary monochromator, and an X'celerator detector. The average crystallite sizes were estimated by the Scherrer equation [86].

2.6.4 N_2 physisorption

Textural analyses were carried out with a Sorptomatic 1990 (Fisons Instruments), by determining the nitrogen adsorption-desorption isotherms at liquid nitrogen temperature. Before analyses, samples were heated overnight under vacuum up to 250 °C (heating rate, 1 °C min^{-1}). Surface area values were calculated by the BET equation. The pore size distribution profiles were determined by applying the non-local DFT method [87,88] (N_2 @ −196 °C on Carbon, Slit Pores model, regularization set to 0.1) to the isotherm adsorption branch in the p/p_0 range 0-0.9. The quality of the obtained isotherm fits is excellent (RMSD as low as 1 cm^3/g), as graphically outlined in Figure S5.

2.6.5 Raman spectroscopy

Raman spectra were acquired by means of a Renishaw inVia Raman microscope instrument with an excitation wavelength of 514 nm. The laser power was fixed at 50% of the maximum power, since the sample in analysis (in the powder form) was kept under motion. The scattered photons were collected through a 20× objective, dispersed by a 1800 lines mm^{-1} grating monochromator and

simultaneously collected on a CCD camera. Each spectrum was obtained by averaging 10 acquisitions with 30 s of exposure each.

2.6.6 Infrared spectroscopy with CO as probe molecule (CO@FT-IR)

FT-IR spectroscopy was performed by means of a Bruker Vertex70 instrument equipped with a Mercury Cadmium Telluride (MCT) detector. Prior to the measurements, pure samples were pressed into self-sustained thin-pellets, placed inside a gold envelope, inserted in a dedicated cell having optical windows in KBr, and heated up to 400 °C under vacuum for 2 h. Then, they were brought to room temperature in vacuum, in order to prevent any surface contamination. After that, CO (30 mbar) was dosed at room temperature as probe molecule and then cooled using liquid nitrogen. FT-IR spectra were obtained by averaging 32 acquisitions with a 2 cm^{-1} resolution during CO desorption *via* volume expansion and afterwards under dynamic vacuum.

2.7 Catalytic tests

Catalytic tests were carried out in a tubular (Φ_{int} = 0.8 cm) quartz-glass fixed-bed continuous-flow microreactor. Prior to reaction the catalyst (0.050 g) was pretreated in N_2 (60 cm^3 min^{-1}) at 400 °C for 5 h. CO oxidation tests were then performed under atmospheric pressure in the temperature range 100-400 °C, with intervals of 50 °C. All tests were performed at a space velocity (*SV*) of 120000 cm^3 h^{-1} g_{cat}^{-1}. A first series of tests was conducted in strong excess of oxygen, by feeding a reactant gas mixture with a CO:O_2 molar ratio equal to 1:4 (CO, 2.0 $\%_{mol}$; O_2, 8.0 $\%_{mol}$; N_2+He, balance). Additional catalytic tests were performed in more severe reaction conditions, by using a stoichiometric CO:O_2 ratio (CO, 2.0 $\%_{mol}$; O_2, 1.0 $\%_{mol}$; N_2+He, balance). Then, in order to simulate the composition of a real gas mixture at the outstream of a combustion process, the catalytic performances of selected samples were studied by adding only CO_2 (CO, 2.0 $\%_{mol}$; O_2, 1.0 $\%_{mol}$; CO_2, 20.0 $\%_{mol}$; N_2+He, balance) or CO_2 and H_2O (CO, 2.0 $\%_{mol}$; O_2, 1.0 $\%_{mol}$; CO_2, 20.0 $\%_{mol}$; H_2O, 9.5 $\%_{mol}$; N_2+He, balance) to the feed. In the presence of water, the catalytic behavior of NiFe/CeO_{2_ht} was also tested by performing a stability test of 40 h at 400 °C. To obtain the desired amount of water

in the reactant gas stream, a vapor generation kit kept at a temperature of 45 °C, was used. Regardless of the composition of the feed, the catalytic performance was monitored at least for 2 h at each temperature, by performing on-line analyses of the reactor effluent on a 6890N (Agilent) gas chromatograph (GC), equipped with an HP PLOT Q capillary column, a methanizer to quantitatively convert CO and CO_2 into methane, and a flame ionization detector (FID). An ice trap and a molecular sieve trap were placed between the reactor and the GC injection valve to condense the water possibly present in the inlet gas mixture. The results of the quantitative analysis of the carbon-containing species were used for checking the carbon mass balance and for calculating CO conversion and CO_2 selectivity.

3. Results and Discussion

3.1. Electron microscopy (SEM, HRTEM)

The templated methods employed to produce the two supports should direct the nanoparticles shape towards different ways. In particular, CTAB employed for CeO_{2_st} synthesis should direct the material form into spheroidal nanoparticles; on the other hand, SBA-15, used to prepare CeO_{2_ht} sample, should push nanoparticles appearance fairly similar to the shape of nanorods. In order to confirm the synthetic outcomes, electron microscopy analyses were performed. The SEM images of soft-templated ceria suggests the presence of clusters due to the agglomeration of fine spheroidal nanoparticles (Figure 1a). Concerning CeO_{2_ht}, instead, much larger and elongated clusters are visible (Figure 1b), consistent with the aggregation of nanosized elongated rods. Since the resolution of SEM microscopy is not sufficiently high to investigate in detail shape and size of fine nanoparticles, HRTEM analyses were also performed (Figure 2).

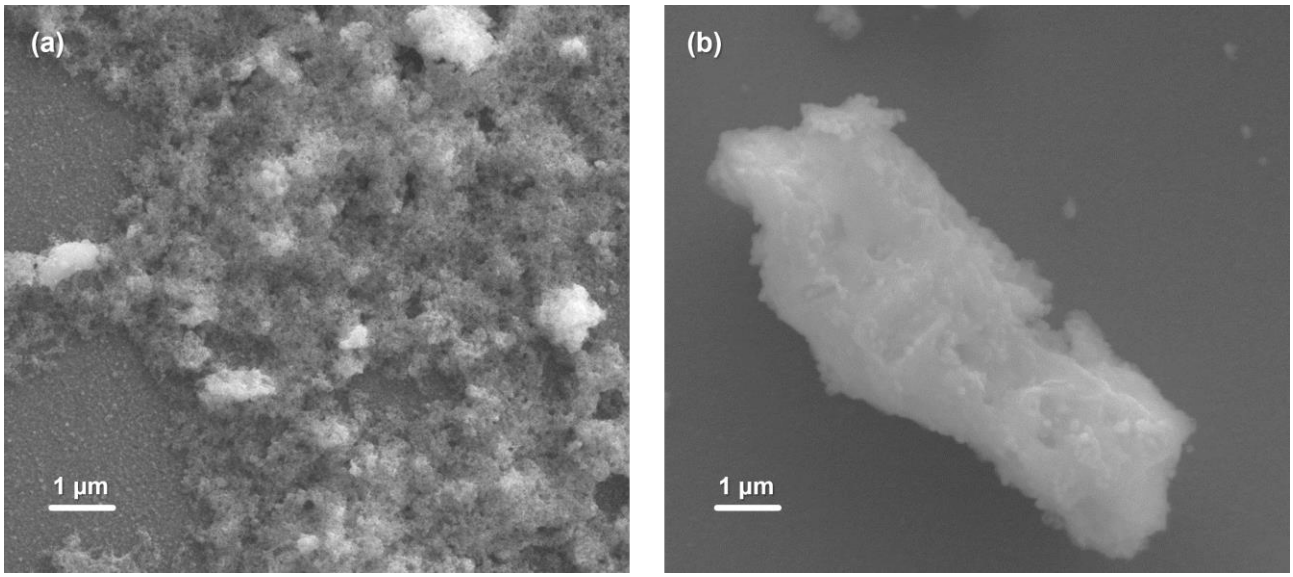

Figure 1. SEM images collected at 10 kx of samples CeO_{2_st} (part a) and CeO_{2_ht} (part b).

Concerning the soft-templated synthesis (Figure 2a), the images confirms the attainment of nanometric-size round-shaped particles, with a 5-10 nm diameter. For the hard-templated synthesis, instead, the image clearly shows an ordered alignment of ceria nanoparticles, having a lateral size compatible with that of the pores of SBA-15 (Figure 2b - inset) [82,89,90]. This evidence indicates the full effectiveness of the hard-templated synthesis.

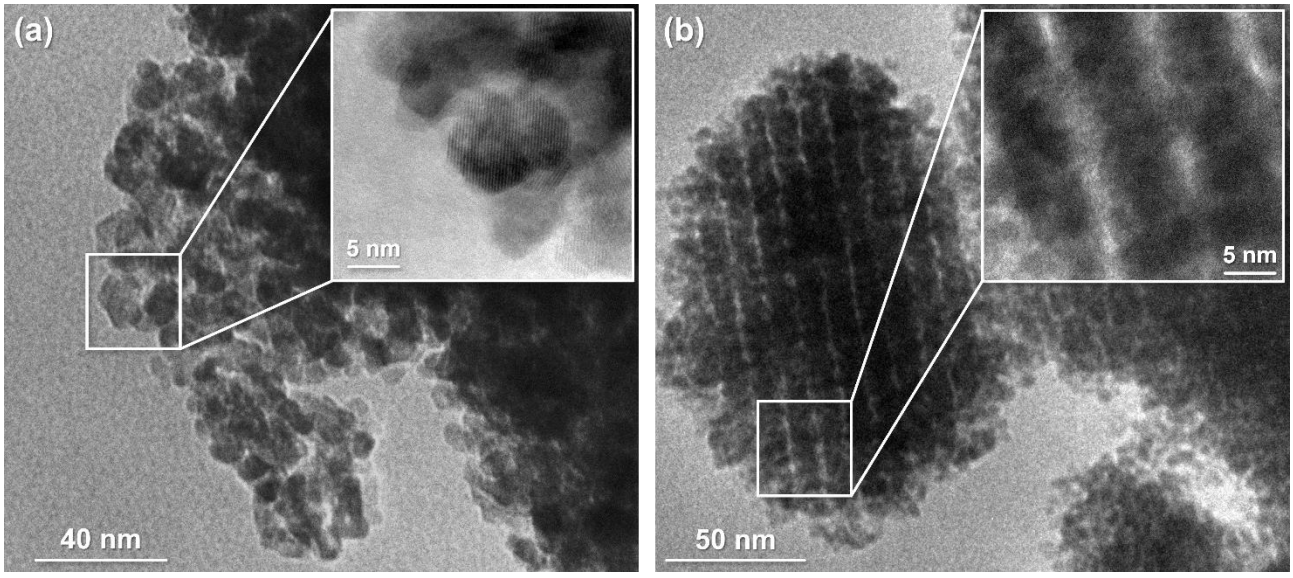

Figure 2. HRTEM images of fresh samples CeO_{2_st} (part a) and CeO_{2_ht} (part b).

3.2. Elemental analysis (ICP-MS, EDX)

Both the supports were used to perform the active phases deposition and the effective metal loading was measured by means of ICP-MS and EDX analyses, and the data are reported in Table 1.

It can be noted that, despite aiming to a hypothetical 5 $\%_{mol}$ of catalytic species loading, only sample Pt/CeO_{2_st} reached such value, while the rest of the samples stayed below that amount. Nevertheless, it was possible to observe a peculiar trend, in which all the catalysts prepared with the hard-template method showed an overall lower metal loading. Such behavior can be ascribed to the ordered honeycomb nanostructure that the hard template conferred to the support, complicating the intimate interaction between the metal precursors and the potential deposition sites along the support surface. This phenomenon gave rise to a slightly lower metal loading with respect to the support in the nanoparticles form obtained with the soft-template method [91]. Concerning the mixed metal samples, the global active phase amount reached only 3.38 $\%_{mol}$ for $NiFe/CeO_{2\_st}$ and 3.11 $\%_{mol}$ for $NiFe/CeO_{2\_ht}$, respectively. However, the Ni:Fe ratio measured in the two catalysts was the same, with a value of 2.6:1, close to the desired 3:1.

Nonetheless, in order to deeply evaluate the synthetic outcomes, a thorough physico-chemical characterization has been performed.

Table 1. ICP-MS and EDX compositional data for the series of catalysts prepared with either hard-templated or soft-templated supports. Data are reported as [($mol_{Metal}/mol_{Support}$) 100]. EDX maps are reported in the supplementary material (Figures S1-S3).

Sample	Fe loading ($\%_{mol}$)	Ni loading ($\%_{mol}$)	Pt loading ($\%_{mol}$)
CeO_{2_st}	-	-	-
$NiFe/CeO_{2\_st}$	0.94/1.09†	2.44/2.46†	-
Ni/CeO_{2_st}	-	3.55	-
Fe/CeO_{2_st}	4.35	-	-
Pt/CeO_{2_st}	-	-	5.49
CeO_{2_ht}	-	-	-
$NiFe/CeO_{2\_ht}$	0.87/0.78†	2.24/2.04†	-
Ni/CeO_{2_ht}	-	2.18	-
Fe/CeO_{2_ht}	3.30	-	-
Pt/CeO_{2_ht}	-	-	3.60

† Value obtained with EDX technique.

3.3. X-Ray Diffraction

XRD patterns of the fresh catalysts prepared by using both the CeO_{2_st} and CeO_{2_ht} supports are reported in Figure 3. Regardless of the ceria used, the diffraction profiles of the Fe-, Ni-, and NiFe-based samples exhibit only reflections ascribable to the typical fluorite-type cubic crystalline structure of cerium oxide (PDF card 75-0151), suggesting a high dispersion of the active phases or that their content is under the detection limit of the technique. As for the two Pt-based samples, while only cerium oxide reflections are visible for Pt/CeO_{2_ht}, a very small signal attributable to metallic Pt^0 (PDF card 04-0802) can be observed for Pt/CeO_{2_st}, which could be explained by considering the slight different contents of platinum in the two samples (Table 1).

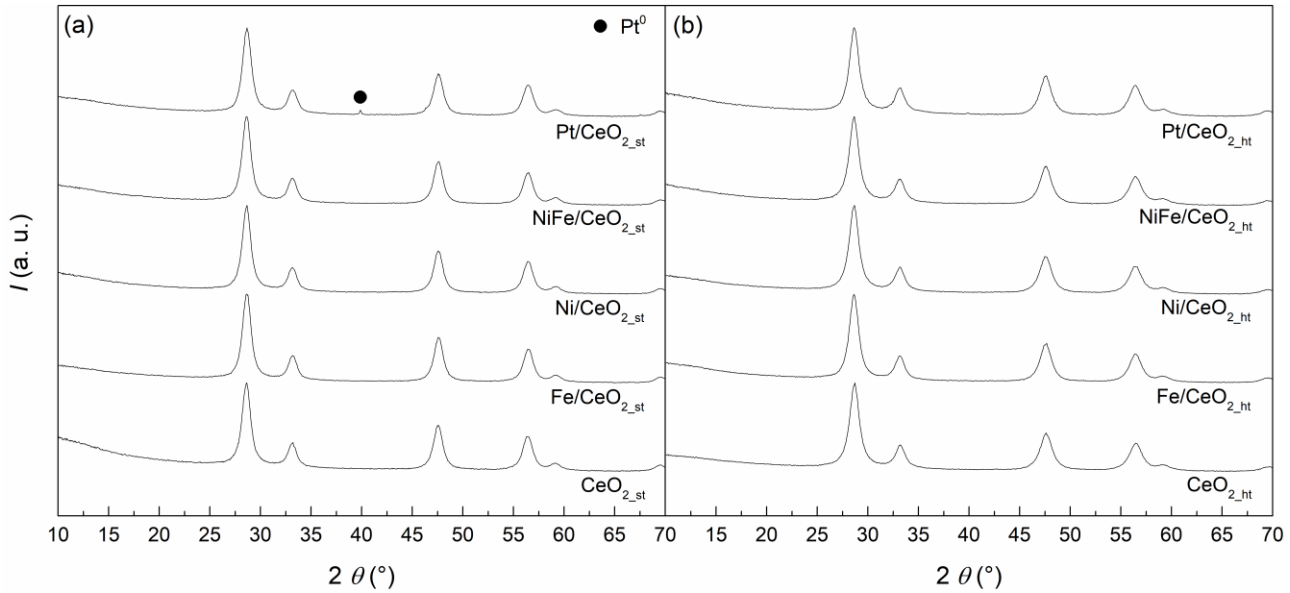

Figure 3. Diffraction patterns of fresh Fe-, Ni-, NiFe-, and Pt-based catalysts supported on CeO_{2_st} (a) and CeO_{2_ht} (b).

CeO_{2_st} and CeO_{2_ht} are characterized by very similar ceria nanocrystals size, for which average diameter values of 7-8 nm have been estimated by the Scherrer equation. As expected, in the case of the hard-templated support, the crystallites size estimated results to be coherent with the mean pore diameter of the pristine SBA-15 used as the template (7.1 nm) [89]. After the impregnation procedure, these values were found unchanged regardless of the active phase nature, thus confirming the high thermal stability of supports.. The XRD profiles of the used catalysts (Figure S4) are quite similar to those the corresponding fresh ones, which did not result significantly different even by varying the composition of the reactant gas mixture.

3.4. N_2 physisorption

The N_2 physisorption isotherms and the pore size distribution (PSD) curves for all the prepared samples are shown in Figure 4, and their textural properties are summarized in Table 2.

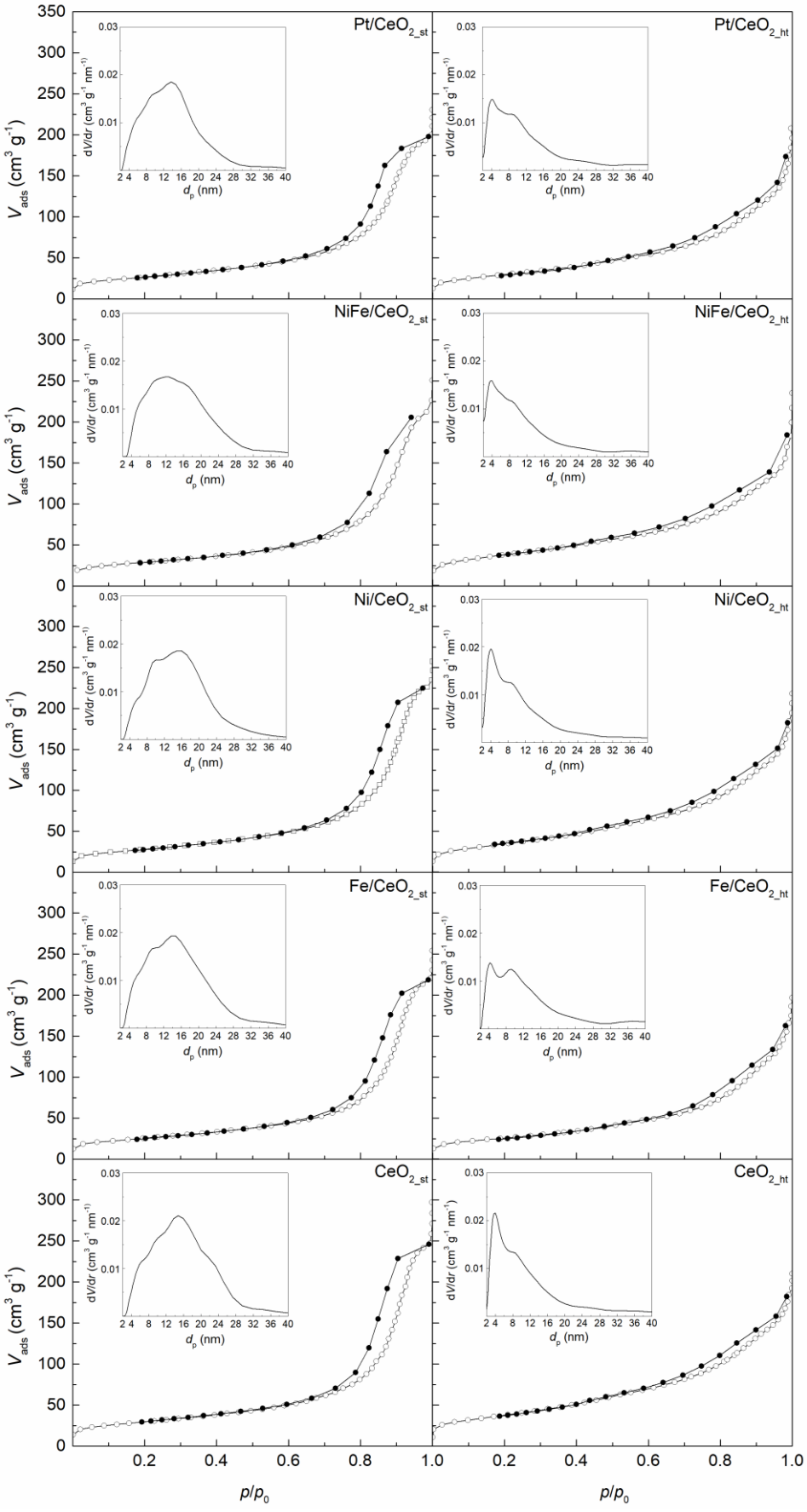

Figure 4. Adsorption-desorption isotherms and pore size distribution (inset) of fresh Fe-, Ni-, NiFe-, and Pt-based catalysts supported on CeO_{2_st} and CeO_{2_ht}.

Table 2. BET specific surface area and total pore volume of CeO_{2_st} and CeO_{2_ht} supported catalysts.

Sample	S_{BET} (m^2 g^{-1})	V_p (cm^3 g^{-1})
CeO_{2_st}	104	0.40
$NiFe/CeO_{2\_st}$	102	0.33
Ni/CeO_{2_st}	100	0.35
Fe/CeO_{2_st}	91	0.34
Pt/CeO_{2_st}	95	0.30
CeO_{2_ht}	136	0.28
$NiFe/CeO_{2\_ht}$	138	0.28
Ni/CeO_{2_ht}	125	0.28
Fe/CeO_{2_ht}	93	0.27
Pt/CeO_{2_ht}	108	0.28

The soft-templated support (CeO_{2_st}) exhibits an adsorption-desorption profile which can be classified as type IVa [92], typical of mesoporous solids. The presence of a hysteresis loop at $p/p_0 > 0.6$ also suggests the potential presence of mesopores, as confirmed by the corresponding PSD plots (insets in Figure 4). The quite broad PSD for soft-templated samples, ranging from 5 to 30 nm, suggests the mesopores are not ordered, thus can be ascribed to interparticle voids in agglomerates. As for CeO_{2_ht}, the isotherms profiles are of type IIb, suggesting a certain degree of interparticle mesoporosity typical of materials prepared with the hard-template method [36,43,92]. Furthermore, the corresponding PSD is sharper than that of CeO_{2_st}. Furthermore, it shows a main peak centered at ca. 3.9 nm, representative for a major family of pores with a size consistent with the value of the pore wall thickness estimated for the SBA-15 [89], highlighting that its topological structure has been, at least partially, replicated during the ceria synthesis. Isotherms profiles and PSD curves of the Fe-, Ni-, NiFe-, and Pt-based catalysts result completely analogous to those of their corresponding support. Irrespective of the ceria used as a support, the impregnation procedure leads to an important decrease

in the surface area (S_{BET}) for both Fe- and Pt-based catalysts, which could suggest a lower dispersion of the active phases probably due to a poorer interaction of the iron and platinum precursors with the ceria surface. Since CeO_{2_ht} exhibits a higher surface area than CeO_{2_st} (Table 2), the higher S_{BET} values of the Ni/CeO_{2_ht}, $NiFe/CeO_{2\_ht}$, and Pt/CeO_{2_ht} materials, in comparison with those of the analogous samples supported on the soft-templated ceria, can be explained accordingly. The sole exception is represented by the Fe-based catalysts, for which the similar S_{BET} values can be justified by a worse dispersion of the iron oxide in the hard-templated ceria [93,94].

3.5. Catalytic behavior and spectroscopic characterization

The overall testing plan began with just CO and O_2 as reactants, similarly to what largely observed in the literature. This was done in order to individuate the most active catalysts to be further tested in progressively more realistic conditions. Catalytic results obtained by feeding CO and O_2 in excess ($CO:O_2$ molar ratio equal to 1:4) are summarized in Figure 5 and Table S1. For each temperature, CO conversion (X_{CO}) is reported as an average of the values determined over 2 h of reaction, within which the catalytic activity was found to be stable. As expected, the only carbon-containing species detected were CO and CO_2, from whose quantification the carbon mass balance was checked.

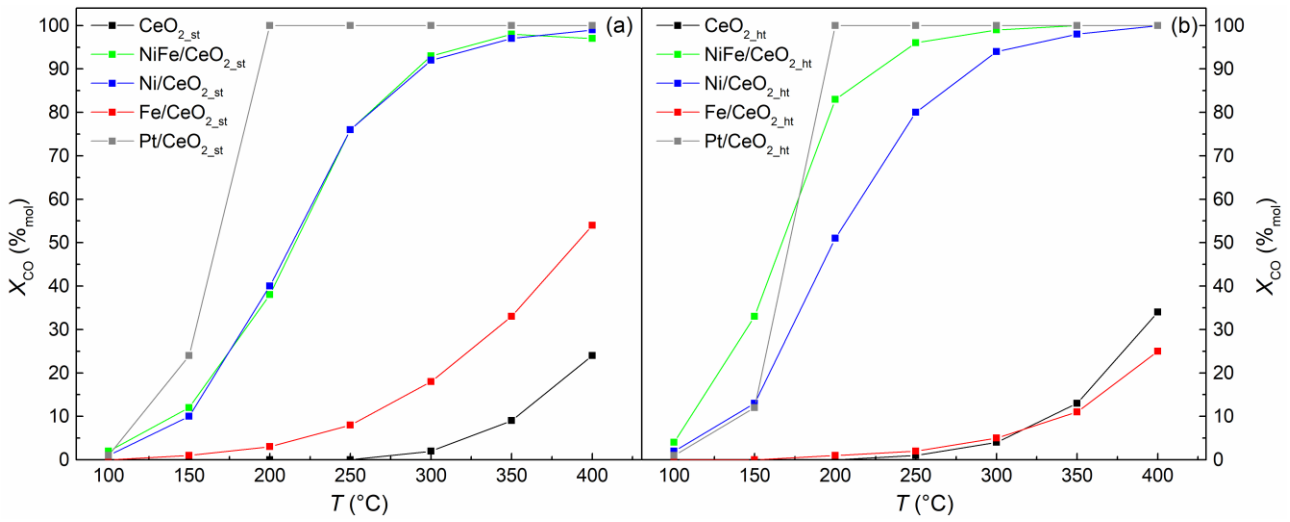

Figure 5. CO conversion (X_{CO}) values as a function of reaction temperature. (a): soft-template series; (b): hard-template series. Space velocity: 120000 $cm^3\ h^{-1}\ g_{cat}^{-1}$; reactant gas composition: CO, 2.0 $\%_{mol}$; O_2, 8.0 $\%_{mol}$; N_2+He, balance.

For each catalyst CO conversion increases with the temperature, although in a different way depending on the nature of the active phase and the type of support. It is worth noticing that at temperature higher than 250 °C pure ceria samples are catalytically active, although to a limited extent. In the literature, CO oxidation on pure ceria is often reported to take place through the Mars-van Krevelen mechanism, in which CO first reacts with surface ceria oxygen forming CO_2 and leaving an oxygen vacancy, which is then filled by oxygen from the gas phase [55]. Between the two ceria supports, the best performance was observed for CeO_{2_ht}, although the maximum X_{CO} barely reaches 34 $\%_{mol}$ at 400 °C. Generally, the presence of additional active species promotes higher activities, meaning that they play a prominent role in the catalytic process. As expected, the Pt-based samples exhibit the best catalytic activity, being able to totally convert CO already at 200 °C. However, at 150 °C a slight higher conversion is observed for Pt/CeO_{2_st}, probably as a consequence of the higher metal content with respect to its hard-templated counterpart (see Table 1). As for the other samples, the best performances are achieved with the NiFe- and Ni-based catalysts, for which, at temperatures ≥ 350 °C, the X_{CO} values are equal or very close to those obtained with the Pt-based samples, highlighting their very promising performance towards the CO oxidation reaction at high temperature. As revealed by ICP-MS and EDX analyses (see Table 1), the materials supported on CeO_{2_ht} are characterized by lower contents of active phase with respect to the corresponding samples of the soft-template series; however, $NiFe/CeO_{2\_ht}$ and Ni/CeO_{2_ht} showed, especially at low and medium temperature, better performance compared with the analogous samples supported on CeO_{2_st}. These results are accordance with those obtained in absence of active phases and suggest a very important role of the support properties in promoting better catalytic performances. As for the Fe-based samples, they turn out to be the worst catalysts irrespective of the support, indicating the crucial role of Ni in obtaining a satisfactory catalytic activity. In particular, Fe/CeO_{2_ht} showed the lowest conversion values, even a little lower than those exhibited by the corresponding pure

hard-templated ceria support. In this case, such behavior can be related to the low Fe content and/or the poor dispersion of iron species, as suggested by N_2 physisorption measurements (see Section 3.4). Since the catalytic results obtained using an excess of oxygen did not allow the identification of a clear trend, we decided to evaluate the performance of the catalysts in more severe conditions, by performing additional tests with O_2 in a stoichiometric amount with respect to CO. The pertinent results, reported in Figure 6 and Table S2, confirm the general trend previously discussed. However, in these conditions, a decrease of the X_{CO} values are observed in the case of NiFe/CeO_{2_st} and Ni/CeO_{2_st}, clearly highlighting the best performances of the NiFe- and Ni-based samples supported on CeO_{2_ht}, for which, instead, the catalytic behavior remains practically the same. Such result further indicates the pivotal role of the hard-templated support, which guarantees a high catalytic activity even in less favorable reaction conditions.

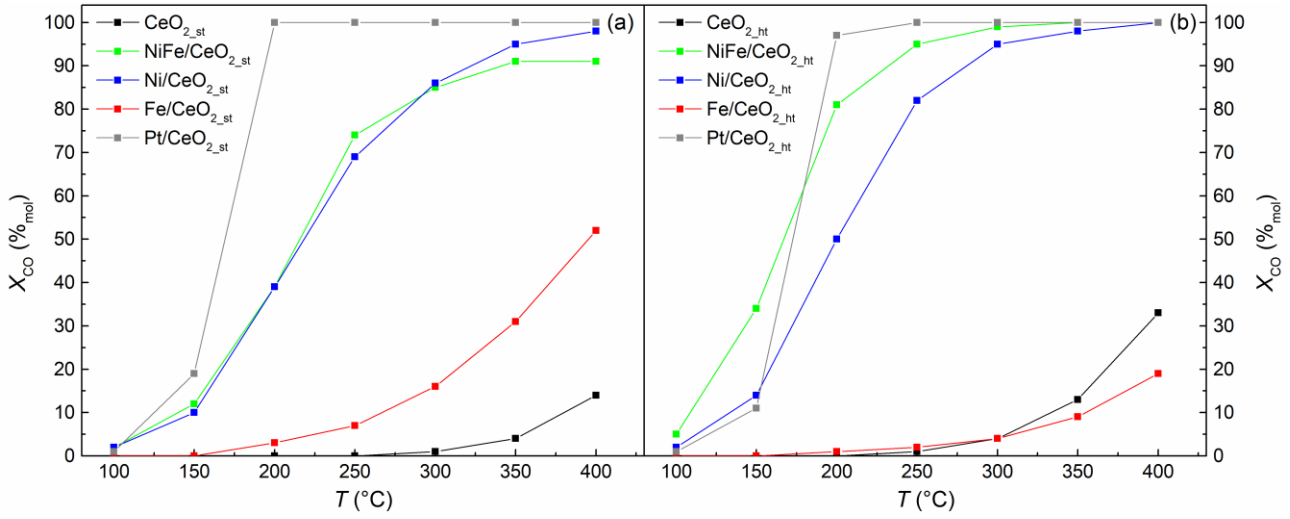

Figure 6. CO conversion (X_{CO}) values as a function of reaction temperature. (a): soft-template series; (b): hard-template series. Space velocity: 120000 cm^3 h^{-1} g_{cat}^{-1}; reactant gas composition: CO, 2.0 $\%_{mol}$; O_2, 1.0 $\%_{mol}$; N_2+He, balance.

In order to investigate the relation between the catalytic performance of the samples and their physical and chemical properties, Raman and CO@FT-IR spectroscopic measurements were performed. Since NiFe/CeO_{2_ht} and Ni/CeO_{2_ht} exhibited the best catalytic activity within all the prepared materials, the series of samples supported on CeO_{2_ht} was investigated. For the sake of comparison with the most

active catalyst ($NiFe/CeO_{2\_ht}$), its counterpart deposited onto the soft-templated support was also studied. Raman spectroscopy can provide information on the structure of the samples. For all the investigated catalysts (Figure 7), it is possible to distinguish an intense signal centered at 462 cm^{-1}, related to the F_{2g} Raman active-mode of fluorite-type cubic structure of CeO_2 [95-97]. This band should shift to lower frequencies when introducing heteroatoms in the structure; interestingly, for all the samples under analysis this effect is not evident, meaning that our active phase is present specifically onto ceria surface as defective site and/or nanoparticles. Instead, the introduction of NiFe- and pure Ni-active phases seems to favor the production of superficial oxygen vacancies, as pointed out by the growth of the signal at 590 cm^{-1} [27,98]. In particular, the amount of such superficial defects results to increase in the order $CeO_{2\_ht} \approx Fe/CeO_{2\_ht} < Ni/CeO_{2\_ht} < NiFe/CeO_{2\_ht}$, which is practically the same trend observed for the catalytic activity (exception made for the soft template support). This evidence is consistent with the direct involvement of the oxygen vacancies in the activation of O_2. Indeed, as suggested in the literature [31], a dual-site mechanism can be assumed when ceria is used as the support in catalytic systems for CO oxidation. In particular, carbon monoxide would be adsorbed on M^0/M^{n+} sites, whereas oxygen could be adsorbed and activated on the defective sites (oxygen vacancies) of ceria. Accordingly, the higher catalytic activity of $NiFe/CeO_{2\_ht}$ could be, at least partially, ascribed to the larger amount of oxygen vacancies. As a confirmation of this, the same correlation can be found also for the NiFe-based samples supported on CeO_{2_ht} and CeO_{2_st}. Indeed, a higher amount of superficial defects can be observed when the active phase is deposited onto the hard-templated support with respect to the soft-templated one (Figure 7b), which is accordance with the better catalytic performance showed by $NiFe/CeO_{2\_ht}$.

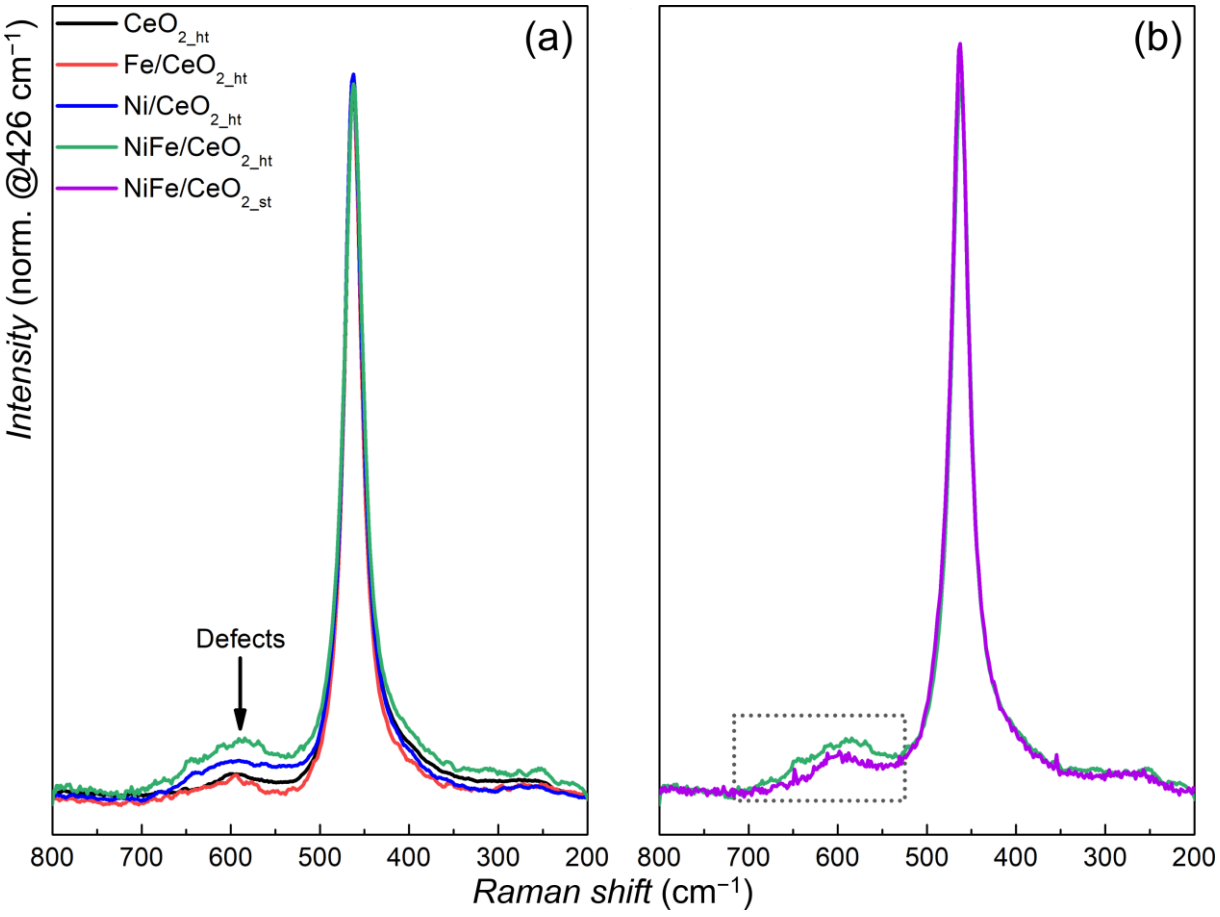

Figure 7. (a) Normalized Raman spectra of fresh CeO_{2_ht}, and fresh Fe-, Ni-, and NiFe-based catalysts supported on CeO_{2_ht}. (b) Comparison between NiFe/CeO_{2_ht} and NiFe/CeO_{2_st}. Dotted box highlights the difference in the superficial defects amount between the two samples.

What could not be probed by Raman spectroscopy is the distribution of the active phase on the surface, either in the form of nanoparticles, or by its possible insertion as a substitutional isolated species, thus provoking a change in the superficial charge responsible for O-vacancies. Nevertheless, we hypothesize that the presence of these vacancies might favor the substitution of Ce^{4+} species from superficial layers of the support with Ni^{2+} ones (also according to Raman data). This fact also justifies their higher catalytic activity. Therefore, in order to demonstrate our supposition, we used a probe molecule coupled with FT-IR spectroscopy might be decisive for understanding the nature of the active species present on the surface of the material. Hence, we studied the CO adsorption at liquid nitrogen temperature by means of FT-IR spectroscopy. Figure 8a and Figure S6 show the vibrational region of carbon monoxide adsorbed onto CeO_{2_ht}-based catalysts.

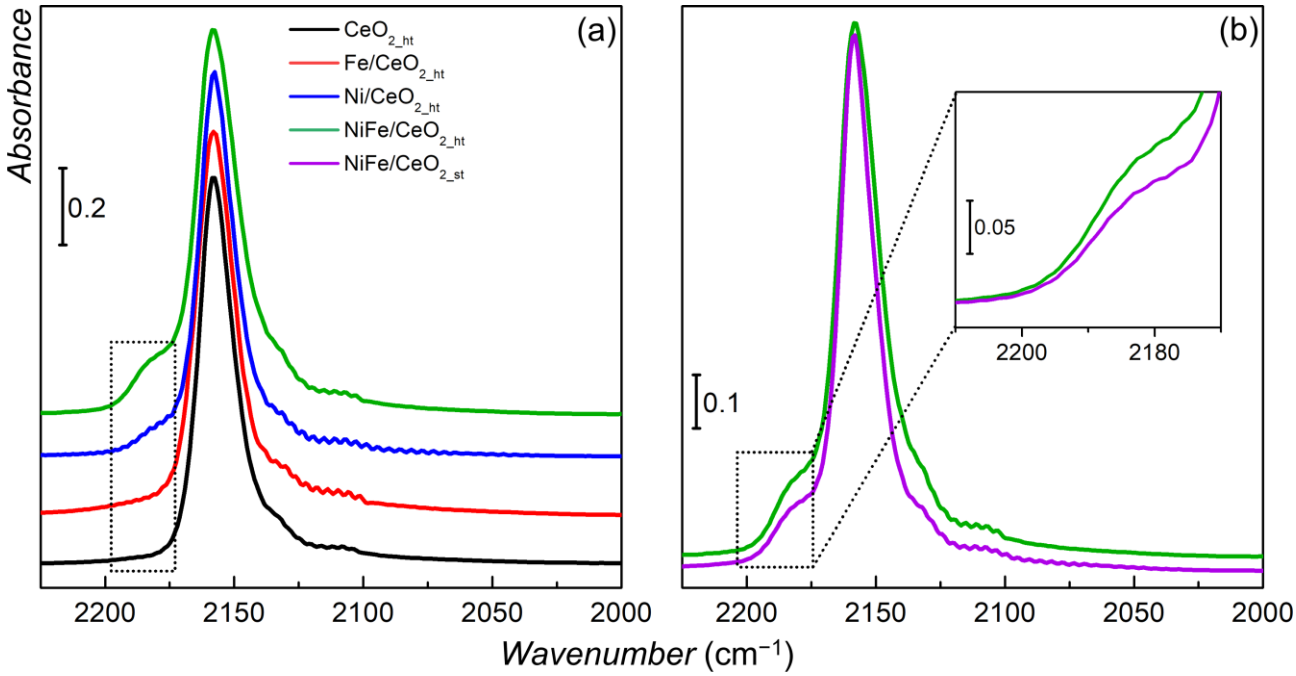

Figure 8. FT-IR spectra of CO adsorbed at liquid N_2 temperature onto (a) fresh CeO_{2_ht}, and fresh Fe-, Ni-, and NiFe-based catalysts supported on CeO_{2_ht}, and (b) onto $NiFe/CeO_{2\_ht}$ and $NiFe/CeO_{2\_st}$. Inset highlights the difference in $CO^{\cdots}Ni^{2+}$ interaction between the samples. Reported spectra are recorded at the maximum CO coverage. Spectra have been normalized to the CO pressure and vertically shifted for the sake of clarity.

All the spectra (Figure 8a) display a major peak centered at 2160 cm^{-1}, generally associated with CO adsorbed end-on on non-defective Ce^{4+} sites ($Ce^{4+\cdots}C{\equiv}O$) present on the surface of the catalysts [99]. Also, all samples display a moderate intensity band at 2125 cm^{-1} due to the presence of a minor amount of superficial Ce^{3+} species [100] (see Figure S6). Another interesting insight is the complete lack of signals below 2100 cm^{-1}, usually related to carbonyls adsorbed on metal nanoparticles. Such signals are also absent upon CO progressive desorption (see Figure S6). This fact, together with the presence of a band at 2180 cm^{-1} (Figure 8a - dotted frame), evidences the extremely high dispersion of the nickel species in the $NiFe/CeO_{2\_ht}$ and Ni/CeO_{2_ht} samples. Indeed, the band at 2180 cm^{-1} is generally associated with the presence of isolated Ni^{2+} cations interacting with CO molecules [101-103]. Despite the excellent agreement in identifying Ni^{2+} species as responsible for the 2180 cm^{-1} signal, also Ce^{4+} uncoordinated sites (CUS) in locally defective CeO_2 can contribute in the same spectral region [104,105], matching the Raman data. Another interesting fact is the absence of any trace of a $Fe^{2+\cdots}CO$ signal at 2195 cm^{-1} [106-108], even for the Fe/CeO_{2_ht} sample (Figure 8a - red

line). These evidences suggest a higher ability of the NiFe- and Ni-based systems in adsorbing and activating CO with respect to the Fe-based one, which – together with the larger amount of oxygen vacancies – could explain the better catalytic performance of the NiFe/CeO_{2_ht} and Ni/CeO_{2_ht} samples. However, iron seems to have a positive effect on the overall exposure of nickel active sites on the surface of NiFe/CeO_{2_ht}. In fact, intriguingly, although NiFe/CeO_{2_ht} and Ni/CeO_{2_ht} have a similar Ni content (see Table 1), the band at 2180 cm^{-1} in the green spectrum in Figure 8a is more intense than that in the blue spectrum (see also Figure S6 where peak fitting is reported in the insets), suggesting an increased amount of surface Ni^{2+} sites in the presence of iron. This phenomenon can be explained with the presence of sub-surface iron species, which are undetectable by probe molecules [109]. Nevertheless, the co-presence of Fe is not the only factor enhancing the exposure of nickel sites. Indeed, NiFe/CeO_{2_ht} (even with a slightly lower metal content - see Table 1) displays a non-negligible larger amount of Ni^{2+} sites available for the reaction with respect to the corresponding sample of the soft-templated series (Figure 8b and also Figure S6, where peak fitting is reported in the insets), meaning that the properties of the support plays a pivotal role. As expected, Raman and FT-IR results suggest how the number of surface Ni^{2+} sites and oxygen vacancies are reciprocally related, the increase of which promotes a superior catalytic activity.

Once pinpointed and characterized the most interesting catalysts, we aimed to investigate their performances in conditions as close as possible to the real ones; therefore, NiFe/CeO_{2_ht} and Ni/CeO_{2_ht} were also tested by adding CO_2 in the gaseous feed mixture (20.0 $\%_{mol}$). The pertinent results are reported in Figure 9 and in Table S3, together with those obtained for Pt/CeO_{2_ht} for the sake of comparison.

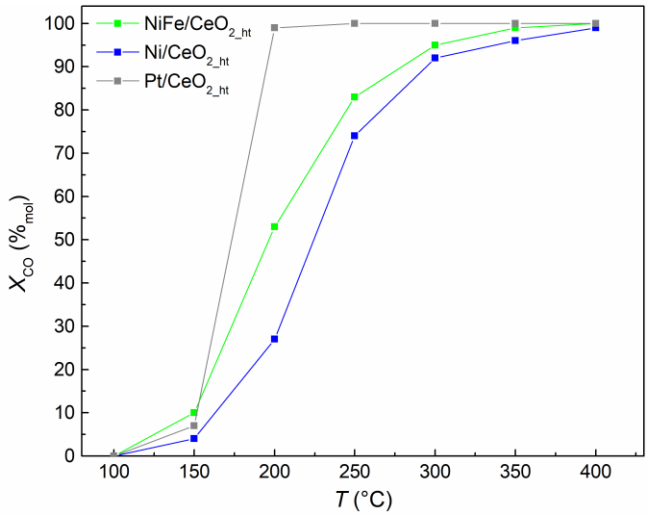

Figure 9. CO conversion (X_{CO}) values as a function of reaction temperature. Space velocity: 120000 $cm^3\ h^{-1}\ g_{cat}^{-1}$; reactant gas composition: CO, 2.0 %$_{mol}$; O_2, 1.0 %$_{mol}$; CO_2, 20.0 %$_{mol}$; N_2+He, balance.

As a consequence of the addition of CO_2 in the feed, a decrease in the X_{CO} values can be observed, especially at temperatures lower than 300 °C (compare with Figure 6 and Table S2). This effect could be tentatively ascribed to kinetic limitations due to competitive adsorption of CO_2 and O_2 on the same O-deficient catalytic sites at lower temperatures. However, such effect become gradually less important as the temperature increases. Indeed, it is well known that CO_2 can be directly adsorbed on the oxygen vacancies of ceria forming stable inorganic carbonate-like species [110]. Between NiFe/CeO_{2_ht} and Ni/CeO_{2_ht}, the first one confirms its superior catalytic performance, especially at low and medium temperatures (Figure 10 and Table S3). However, at temperatures ≥ 350 °C both the samples exhibit CO conversions very close or equal (in the case of NiFe/CeO_{2_ht}) to those found for the Pt-based sample (100 %$_{mol}$).

Since, besides CO_2, water is also present in real combustion exhausts, the most promising catalyst (namely NiFe/CeO_{2_ht}) was also tested with the simultaneous presence of CO_2 and H_2O (20.0 %$_{mol}$ and 9.5 %$_{mol}$, respectively) in the gaseous feed mixture (Figure 10 and Table S4). The selected feed composition was chosen to simulate a real reaction environment [81].

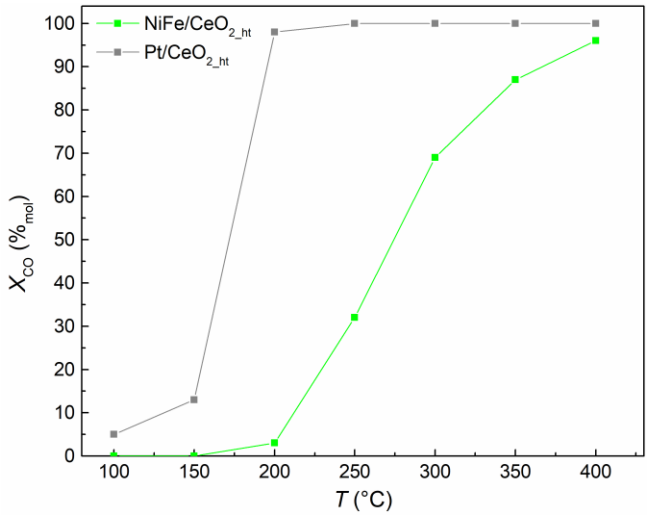

Figure 10. CO conversion (X_{CO}) values as a function of reaction temperature. Space velocity: 120000 $cm^3\ h^{-1}\ g_{cat}^{-1}$; reactant gas composition: CO, 2.0 $\%_{mol}$; O_2, 1.0 $\%_{mol}$; CO_2, 20.0 $\%_{mol}$; H_2O, 9.5 $\%_{mol}$; N_2+He, balance.

The addition of water significantly affects the catalytic performance of $NiFe/CeO_{2\_ht}$, especially at low and medium temperatures (100-300 °C). In the literature, the detrimental effect of water towards the performance of Co_3O_4 and CuO/CeO_2 has been reported in a few papers [111,112]. In the case of cobalt oxide, the authors found that the presence of water during the catalyst pretreatment caused a significant increase in the kinetic order with respect to CO, suggesting a competitive adsorption between H_2O and CO for the same catalytic sites [111]. On CuO/CeO_2 the inhibiting effect of water was ascribed to the formation of surface $Cu(OH)_2$, which limited the adsorption of CO on the Cu species responsible for its activation [112]. On this base, although more detailed studies are needed in order to better investigate the role of water, the decrease in CO conversion observed in the case of $NiFe/CeO_{2\_ht}$ could be tentatively ascribed to the competitive adsorption of H_2O and CO for the same Ni^{2+} sites. Nevertheless, once again, very high CO conversions are found at the highest temperatures (X_{CO} is equal to 96 $\%_{mol}$ at 400 °C), indicating that, also in these more severe reaction conditions, the $NiFe/CeO_{2\_ht}$ sample is a very promising catalyst for the CO conversion to CO_2 at operating temperatures closely resembling the one of exhausts. In addition, to investigate its catalytic behavior in terms of stability, $NiFe/CeO_{2\_ht}$ was tested at 400 °C for 40 h. The results (Table S5) highlight an

outstanding stability of NiFe/CeO_{2_ht} catalyst even in extremely harsh reaction conditions, with the X_{co} values stably remaining at 94 $\%_{mol}$ at the end of the test.

4. Conclusions

In the search for more competitive catalysts to reduce economic impact, still maintaining excellent performances, we prepared, characterized, and tested several ceria-supported transition metal catalysts, aiming to substitute costly noble metals in the carbon monoxide abatement from industrial and powerplant exhausts. We successfully obtained NiFe-, Ni- and Fe-based materials supported on both soft-templated and hard-templated ceria. Even though the catalytic activity of all materials was way lower than that of a platinum-based one below 300 °C, the nickel-iron mixed metal catalyst prepared with the hard-templated ceria support exhibited conversion values comparable to the platinum-based catalyst at the actual operating temperature range reached by combustion gases when released in the atmosphere (350-400 °C). We identified the key of their excellent performances in the synergy between O-vacancies generated in the proximity of Ni^{2+} superficial substitutional defects. Indeed, the missing oxygen is responsible for O_2 activation, thus maximizing the catalytic activity even in the least favorable reaction environment. This allowed us to keep not only the temperature but also the feed composition as close as possible to the real operating conditions, leaving the performance of our best material almost unaffected. The achieved results would allow our catalyst to replace noble metal ones, still respecting the new EU Directives in terms of polluting emissions from industrial activities.

Acknowledgements

Thanks are due to Andrea Ardu and to the ‘Centro Servizi di Ateneo per la Ricerca (CeSAR)’ of the University of Cagliari for the TEM/EDX and HRTEM measurements performed with a JEOL JEM 1400-PLUS and a JEOL JEM 2010 UHR microscopes. MS acknowledges support from the Project CH4.0 under the MUR program "Dipartimenti di Eccellenza 2023-2027" (CUP: D13C22003520001). AL and MC acknowledge the funding by the European Union - NextGenerationEU under the Italian

Ministry of University and Research (MUR) National Innovation Ecosystem grant ECS00000041 - VITALITY (CUP: E13C22001060006).

References

1. Choudhary, S.; Saalim, S.M.; Khare, N. Chapter 1 - Climate change over the Arctic: impacts and assessment. In *Understanding Present and Past Arctic Environments*, Khare, N., Ed.; Elsevier: **2021**; pp. 1-14.
2. United Nations World Cities Report 2022: Envisaging the Future of Cities.
3. Directive (EU) 2015/2193 of the European Parliament and of the Council of 25 November 2015 on the limitation of emissions of certain pollutants into the air from medium combustion plants, http://data.europa.eu/eli/dir/2015/2193/oj.
4. Omaye, S.T., Metabolic modulation of carbon monoxide toxicity, Toxicology, 180 (2002) 139-150.
5. Tikuisis, P.; Kane, D.M.; McLellan, T.M.; Buick, F.; Fairburn, S.M., Rate of formation of carboxyhemoglobin in exercising humans exposed to carbon monoxide, J. Appl. Physiol., 72 (1992) 1311-1319.
6. Vasquez, G.B.; Ji, X.H.; Fronticelli, C.; Gilliland, G.L., Human Carboxyhemoglobin at 2.2 Å Resolution: Structure and Solvent Comparisons of R-State, R2-State and T-State Hemoglobins, Acta Crystallogr. D: Biol. Crystallogr., 54 (1998) 355-366.
7. Dey, S.; Dhal, G.C., Materials progress in the control of CO and CO_2 emission at ambient conditions: An overview, Mater Sci Energy Technol, 2 (2019) 607-623.
8. Blumenthal, I., Carbon Monoxide Poisoning, J. R. Soc. Med., 94 (2001) 270-272.
9. Hofmann, G.; Rochet, A.; Ogel, E.; Casapu, M.; Ritter, S.; Ogurreck, M.; Grunwaldt, J.-D., Aging of a Pt/Al_2O_3 exhaust gas catalyst monitored by quasi in situ X-ray micro computed tomography, RSC Adv., 5 (2015) 6893-6905.
10. He, L.; Fan, Y.; Luo, L.; Bellettre, J.; Yue, J., Preparation of $Pt/\gamma\text{-}Al_2O_3$ catalyst coating in microreactors for catalytic methane combustion, Chem. Eng. J., 380 (2020) 122424.
11. Chawla, J.; Schardt, S.; Angeli, S.; Lott, P.; Tischer, S.; Maier, L.; Deutschmann, O., Oxidative Coupling of Methane over Pt/Al_2O_3 at High Temperature: Multiscale Modeling of the Catalytic Monolith, Catalysts, 12 (2022) 189.
12. Carlsson, P.A.; Osterlund, L.; Thormahlen, P.; Palmqvist, A.; Fridell, E.; Jansson, J.; Skoglundh, M., A transient in situ FTIR and XANES study of CO oxidation over Pt/Al_2O_3 catalysts, J. Catal., 226 (2004) 422-434.
13. Chen, Y.; Feng, Y.X.; Li, L.; Liu, J.Y.; Pan, X.L.; Liu, W.; Wei, F.F.; Cui, Y.T.; Qiao, B.T.; Sun, X.C.; Li, X.Y.; Lin, J.; Lin, S.; Wang, X.D.; Zhang, T., Identification of Active Sites on

High-Performance Pt/Al_2O_3 Catalyst for Cryogenic CO Oxidation, ACS Catal., 10 (2020) 8815-8824.

14. Ivanova, A.S.; Slavinskaya, E.M.; Gulyaev, R.V.; Zaikovskii, V.I.; Stonkus, O.A.; Danilova, I.G.; Plyasova, L.M.; Polukhina, I.A.; Boronin, A.I., Metal-support interactions in Pt/Al_2O_3 and Pd/Al_2O_3 catalysts for CO oxidation, Appl. Catal. B: Environ., 97 (2010) 57-71.

15. Kahlich, M.J.; Gasteiger, H.A.; Behm, R.J., Kinetics of the selective CO oxidation in H_2-rich gas on Pt/Al_2O_3, J. Catal., 171 (1997) 93-105.

16. Mozer, T.S.; Passos, F.B., Selective CO oxidation on Cu promoted Pt/Al_2O_3 and Pt/Nb_2O_5 catalysts, Int. J. Hydrog. Energy, 36 (2011) 13369-13378.

17. Vleephoka, C.; Chaisuk, C.; Samparnpiboon, P.; Praserthdam, P., Effect of phase composition between nano g- and c-Al_2O_3 on Pt/Al_2O_3 catalyst in CO oxidation, Catal. Commun., 9 (2008) 546-550.

18. Bowker, M.; Nuhu, A.; Soares, J., High activity supported gold catalysts by incipient wetness impregnation, Catal. Today, 122 (2007) 245-247.

19. Zhu, H.Q.; Qin, Z.F.; Shan, W.J.; Shen, W.J.; Wang, J.G., Pd/CeO_2-TiO_2 catalyst for CO oxidation at low temperature: a TPR study with H_2 and CO as reducing agents, J. Catal., 225 (2004) 267-277.

20. Aneggi, E.; Rico-Perez, V.; de Leitenburg, C.; Maschio, S.; Soler, L.; Llorca, J.; Trovarelli, A., Ceria-Zirconia Particles Wrapped in a 2D Carbon Envelope: Improved Low-Temperature Oxygen Transfer and Oxidation Activity, Angew. Chem.-Int. Edit., 54 (2015) 14040-14043.

21. Bunluesin, T.; Putna, E.S.; Gorte, R.J., A comparison of CO oxidation on ceria-supported Pt, Pd, and Rh, Catal. Lett., 41 (1996) 1-5.

22. Chang, L.H.; Sasirekha, N.; Rajesh, B.; Chen, Y.W., CO oxidation on ceria- and manganese oxide-supported gold catalysts, Sep. Purif. Technol., 58 (2007) 211-218.

23. Chung, L.C.; Yeh, C.T., Synthesis of highly active CuO-CeO_2 nanocomposites for preferential oxidation of carbon monoxide at low temperatures, Catal. Commun., 9 (2008) 670-674.

24. Gatla, S.; Aubert, D.; Agostini, G.; Mathon, O.; Pascarelli, S.; Lunkenbein, T.; Willinger, M.G.; Kaper, H., Room-Temperature CO Oxidation Catalyst: Low-Temperature Metal-Support Interaction between Platinum Nanoparticles and Nanosized Ceria, ACS Catal., 6 (2016) 6151-6155.

25. Kim, H.J.; Jang, M.G.; Shin, D.; Han, J.W., Design of Ceria Catalysts for Low-Temperature CO Oxidation, ChemCatChem, 12 (2020) 11-26.

26. Zhang, X.; Su, L.F.; Kong, Y.L.; Ma, D.; Ran, Y.; Peng, S.J.; Wang, L.H.; Wang, Y.D., CeO_2 nanoparticles modified by CuO nanoparticles for low-temperature CO oxidation with high catalytic activity, J. Phys. Chem. Solids, 147 (2020) 109651.

27. Manzoli, M.; Avgouropoulos, G.; Tabakova, T.; Papavasiliou, J.; Ioannides, T.; Boccuzzi, F., Preferential CO oxidation in H_2-rich gas mixtures over Au/doped ceria catalysts, Catal. Today, 138 (2008) 239-243.

28. Pozdnyakova, O.; Teschner, D.; Wootsch, A.; Kröhnert, J.; Steinhauer, B.; Sauer, H.; Toth, L.; Jentoft, F.C.; Knop-Gericke, A.; Paál, Z.; Schlögl, R., Preferential CO oxidation in hydrogen (PROX) on ceria-supported catalysts, part I: Oxidation state and surface species on Pt/CeO_2 under reaction conditions, J. Catal., 237 (2006) 1-16.

29. Kaspar, J.; Fornasiero, P.; Graziani, M., Use of CeO_2-based oxides in the three-way catalysis, Catal. Today, 50 (1999) 285-298.

30. Lazzarini, A.; Colaiezzi, R.; Gabriele, F.; Crucianelli, M., Support-Activity Relationship in Heterogeneous Catalysis for Biomass Valorization and Fine-Chemicals Production, Materials, 14 (2021) 6796.

31. Royer, S.; Duprez, D., Catalytic Oxidation of Carbon Monoxide over Transition Metal Oxides, ChemCatChem, 3 (2011) 24-65.

32. Portillo-Velez, N.S.; Zanella, R., Comparative study of transition metal (Mn, Fe or Co) catalysts supported on titania: Effect of Au nanoparticles addition towards CO oxidation and soot combustion reactions, Chem. Eng. J., 385 (2020) 123848.

33. Thormählen, P.; Skoglundh, M.; Fridell, E.; Andersson, B., Low-Temperature CO Oxidation over Platinum and Cobalt Oxide Catalysts, J. Catal., 188 (1999) 300-310.

34. Varghese, S.; Cutrufello, M.G.; Rombi, E.; Cannas, C.; Monaci, R.; Ferino, I., CO oxidation and preferential oxidation of CO in the presence of hydrogen over SBA-15-templated CuO-Co_3O_4 catalysts, Appl. Catal. A: Gen., 443 (2012) 161-170.

35. Lima, T.M.; de Macedo, V.; Silva, D.S.A.; Castelblanco, W.N.; Pereira, C.A.; Roncolatto, R.E.; Gawande, M.B.; Zboril, R.; Varma, R.S.; Urquieta-Gonzalez, E.A., Molybdenum-promoted cobalt supported on SBA-15: Steam and sulfur dioxide stable catalyst for CO oxidation, Appl. Catal. B: Environ., 277 (2020) 119248.

36. Wang, Y.; Wang, Y.; Ren, J.; Mi, Y.; Zhang, F.; Li, C.; Liu, X.; Guo, Y.; Guo, Y.; Lu, G., Synthesis of morphology-controllable mesoporous Co_3O_4 and CeO_2, J. Solid State Chem., 183 (2010) 277-284.

37. Mohamad, M.F.; Ramli, A.; Yusup, S., Study on the physicochemical properties of Fe/CeO_2 catalysts as an effect from different iron loading, AIP Conf. Proc., 1502 (2012) 288-297.

38. Tan, L.; Tao, Q.; Gao, H.Y.; Li, J.; Jia, D.D.; Yang, M., Preparation and catalytic performance of mesoporous ceria-base composites CuO/CeO_2, Fe_2O_3/CeO_2 and La_2O_3/CeO_2, J. Porous Mater., 24 (2017) 795-803.

39. Wang, X.F.; Jin, B.T.; He, X.Q.; White, T.A.; Liang, X.H., Highly Active and Stable Fe/SiO_2 Catalyst Synthesized by Atomic Layer Deposition for CO Oxidation, Catal. Lett., 150 (2020) 3296-3303.

40. Yu, S.; Yun, H.J.; Lee, D.M.; Yi, J., Preparation and characterization of Fe-doped TiO_2 nanoparticles as a support for a high performance CO oxidation catalyst, J. Mater. Chem., 22 (2012) 12629-12635.

41. Atzori, L.; Cutrufello, M.G.; Meloni, D.; Cannas, C.; Gazzoli, D.; Monaci, R.; Sini, M.F.; Rombi, E., Highly active NiO-CeO_2 catalysts for synthetic natural gas production by CO_2 methanation, Catal. Today, 299 (2018) 183-192.

42. Atzori, L.; Rombi, E.; Meloni, D.; Sini, M.F.; Monaci, R.; Cutrufello, M.G., CO and CO_2 Co-Methanation on Ni/CeO_2-ZrO_2 Soft-Templated Catalysts, Catalysts, 9 (2019) 415.

43. Rombi, E.; Cutrufello, M.G.; Atzori, L.; Monaci, R.; Ardu, A.; Gazzoli, D.; Deiana, P.; Ferino, I., CO methanation on Ni-Ce mixed oxides prepared by hard template method, Appl. Catal. A: Gen., 515 (2016) 144-153.

44. Chen, L.M.; Bao, Y.F.; Sun, Y.H.; Ma, D.; Ye, D.Q.; Huang, B.C., The graphitic carbon strengthened synergetic effect between Pt and FeNi in CO preferential oxidation in excess hydrogen at low temperature, Catal. Sci. Technol., 6 (2016) 98-106.

45. Jha, A.; Jeong, D.W.; Jang, W.J.; Rode, C.V.; Roh, H.S., Mesoporous NiCu-CeO_2 oxide catalysts for high-temperature water-gas shift reaction, RSC Adv., 5 (2015) 1430-1437.

46. Varghese, S.; Cutrufello, M.G.; Rombi, E.; Monaci, R.; Cannas, C.; Ferino, I., Mesoporous hard-templated Me-Co [Me = Cu, Fe] spinel oxides for water gas shift reaction, J. Porous Mat., 21 (2014) 539-549.

47. Wang, W.; Chai, D.; Yang, Y.; Liu, Y.Q.; Kang, Y.M.; Lei, Z.Q., Fe-Co hybrid oxides promoted Pd electrocatalysts with enhanced catalytic performance for ethylene glycol oxidation, Int. J. Hydrog. Energy, 40 (2015) 10041-10048.

48. Wang, X.; Du, L.Y.; Du, M.; Ma, C.; Zeng, J.; Jia, C.J.; Si, R., Catalytically active ceria-supported cobalt-manganese oxide nanocatalysts for oxidation of carbon monoxide, Phys. Chem. Chem. Phys., 19 (2017) 14533-14542.

49. Peymani, M.; Alavi, S.M.; Arandiyan, H.; Rezaei, M., Rational Design of High Surface Area Mesoporous Ni/CeO_2 for Partial Oxidation of Propane, Catalysts, 8 (2018) 388.

50. Peymani, M.; Alavi, S.M.; Rezaei, M., Preparation of highly active and stable nanostructured Ni/CeO_2 catalysts for syngas production by partial oxidation of methane, Int. J. Hydrog. Energy, 41 (2016) 6316-6325.

51. Wu, H.Q.; Qian, C.; Cao, Y.J.; Cao, P.P.; Li, W.T.; Zhang, X.J.; Wei, X.W., Synthesis and magnetic properties of size-controlled FeNi alloy nanoparticles attached on multiwalled carbon nanotubes, J. Phys. Chem. Solids, 71 (2010) 290-295.

52. Li, J.; Zhang, D.; Qi, H.; Wang, G.M.; Tang, J.M.; Tian, G.; Liu, A.H.; Yue, H.J.; Yu, Y.; Feng, S.H., Economical synthesis of composites of FeNi alloy nanoparticles evenly dispersed in two-dimensional reduced graphene oxide as thin and effective electromagnetic wave absorbers, RSC Adv., 8 (2018) 8393-8401.

53. Silman, G.I., Compilative Fe-Ni phase diagram with author's correction, Met. Sci. Heat Treat., 54 (2012) 105-112.

54. Ghiami, S.; Nasseri, M.A.; Allahresani, A.; Kazemnejadi, M., $FeNi_3$@SiO_2 nanoparticles: an efficient and selective heterogeneous catalyst for the epoxidation of olefins and the oxidation of sulfides in the presence of meta-chloroperoxybenzoic acid at room temperature, React. Kinet. Mech. Catal., 126 (2019) 383-398.

55. Trovarelli, A.; Llorca, J., Ceria Catalysts at Nanoscale: How Do Crystal Shapes Shape Catalysis?, ACS Catal., 7 (2017) 4716-4735.

56. Li, H.F.; Lu, G.Z.; Dai, Q.G.; Wang, Y.Q.; Guo, Y.; Guo, Y.L., Hierarchical Organization and Catalytic Activity of High-Surface-Area Mesoporous Ceria Microspheres Prepared Via Hydrothermal Routes, ACS Appl. Mater. Interfaces, 2 (2010) 838-846.

57. Fu, X.H.; Liu, Y.X.; Deng, J.G.; Jing, L.; Zhang, X.; Zhang, K.F.; Han, Z.; Jiang, X.Y.; Dai, H.X., Intermetallic compound PtMny-derived Pt - MnOx supported on mesoporous CeO2: Highly efficient catalysts for the combustion of toluene, Appl. Catal. A: Gen., 595 (2020) 117509.

58. Lin, B.F.; Lei, Z.; Xu, F.; Cheng, N.C.; Mu, S.C., Poly(vinylpyrrolidone) tailored porous ceria as a carbon-free support for methanol electrooxidation, Electrochim. Acta, 290 (2018) 55-62.

59. Lu, B.W.; Li, Z.Y.; Kawamoto, K., Synthesis of mesoporous ceria without template, Mater. Res. Bull., 48 (2013) 2504-2510.

60. Akinnawo, C.A.; Bingwa, N.; Meijboom, R., Tailoring the surface properties of meso-CeO_2 for selective oxidation of benzyl alcohol, Catal. Commun., 145 (2020) 106115.

61. Zhou, K.B.; Yang, Z.Q.; Yang, S., Highly reducible CeO_2 nanotubes, Chem. Mater., 19 (2007) 1215-1217.

62. Eaimsumang, S.; Chollacoop, N.; Luengnaruemitchai, A.; Taylor, S.H., Ceria nanorod supported gold nanoparticles as structured catalysts for the oxidative steam reforming of methanol: Effect of CTAB concentration on physiochemical properties and catalyst performance, J. Catal., 392 (2020) 254-265.

63. Kurajica, S.; Minga, I.; Gulis, M.; Mandic, V.; Simcic, I., High Surface Area Ceria Nanoparticles via Hydrothermal Synthesis Experiment Design, J. Nanomater., 2016 (2016) 7274949.

64. Sahoo, S.K.; Mohapatra, M.; Singh, A.K.; Anand, S., Hydrothermal Synthesis of Single Crystalline Nano CeO_2 and Its Structural, Optical, and Electronic Characterization, Mater. Manuf. Process., 25 (2010) 982-989.

65. Pal, N.; Cho, E.B.; Patra, A.K.; Kim, D., Ceria-Containing Ordered Mesoporous Silica: Synthesis, Properties, and Applications, ChemCatChem, 8 (2016) 285-303.

66. Pal, N.; Cho, E.B.; Kim, D.; Gunathilake, C.; Jaroniec, M., Catalytic activity of $Ce^{IV}O_2/Ce_2^{III}O_3$-silica mesoporous composite materials for oxidation and esterification reactions, Chem. Eng. J., 262 (2015) 1116-1125.

67. Vargas, O.A.G.; Heredia, J.A.D.; Suarez-Toriello, V.A.; Rangel, R.H.; Wang, J.A.; Chen, L.F., Characterization of structural and optical properties of the mesoporous Ce-MCM-41 hybrid materials, J. Mater. Sci. Mater. Electron., 29 (2018) 15621-15631.

68. Vargas, O.A.G.; Heredia, J.A.D.; Castellanos, A.M.; Chen, L.F.; Wang, J.A., Cerium incorporating into MCM-41 mesoporous materials for CO oxidation, Mater. Chem. Phys., 139 (2013) 125-133.

69. Mitran, R.A.; Culita, D.C.; Atkinson, I., Thermal stability enhancement of mesoporous SBA-15 silica through nanoconfinement of ceria nanoparticles, Microporous Mesoporous Mater., 306 (2020).

70. Pal, N.; E.-B., C.; D., K., Synthesis of ordered mesoporous silica/ceria–silica composites and their high catalytic performance for solvent-free oxidation of benzyl alcohol at room temperature, RSC Adv., 4 (2014) 9213-9222.

71. Lolli, A.; Amadori, R.; Lucarelli, C.; Cutrufello, M.G.; Rombi, E.; Cavani, F.; Albonetti, S., Hard-template preparation of Au/CeO_2 mesostructured catalysts and their activity for the selective oxidation of 5-hydroxymethylfurfural to 2,5-furandicarboxylic acid, Microporous Mesoporous Mater., 226 (2016) 466-475.

72. Miller, B.K.; Crozier, P.A., Linking Changes in Reaction Kinetics and Atomic-Level Surface Structures on a Supported Ru Catalyst for CO Oxidation, ACS Catal., 11 (2021) 1456-1463.

73. Gao, Y.; Chiang, F.-K.; Li, S.; Zhang, L.; Wang, P.; Hensen, E.J.M., Influence of hematite morphology on the CO oxidation performance of $Au/\alpha\text{-}Fe_2O_3$, Chinese J. Catal., 42 (2021) 658-665.

74. Che-Galicia, G.; Ruíz-Santoyo, V.; Zanella, R.; Mendoza-González, N.Y.; Ruiz-López, I.I.; Sampieri, A., Kinetic mechanism of CO oxidation on gold catalyst supported on TiSBA-15 previously treated in a hydrogen atmosphere, Chem. Eng. J., 405 (2021) 126644.

75. Al Soubaihi, R.M.; Saoud, K.M.; Myint, M.T.Z.; Gothelid, M.A.; Dutta, J., CO Oxidation Efficiency and Hysteresis Behavior over Mesoporous Pd/SiO_2 Catalyst, Catalysts, 11 (2021) 131.

76. Zhang, S.R.; An, K.; Li, S.S.; Zhang, Z.Y.; Sun, R.L.; Liu, Y., Bi-active sites of stable and highly dispersed platinum and oxygen vacancy constructed by reducing a loaded perovskite-type oxide for CO oxidation, Appl. Surf. Sci., 532 (2020) 147455.

77. Slavinskaya, E.M.; Zadesenets, A.V.; Stonkus, O.A.; Stadnichenko, A.I.; Shchukarev, A.V.; Shubin, Y.V.; Korenev, S.V.; Boronin, A.I., Thermal activation of $Pd/CeO_2\text{-}SnO_2$ catalysts for low-temperature CO oxidation, Appl. Catal. B: Environ., 277 (2020) 119275.

78. Liu, X.; Jia, S.F.; Yang, M.; Tang, Y.T.; Wen, Y.W.; Chu, S.Q.; Wang, J.B.; Shan, B.; Chen, R., Activation of subnanometric Pt on Cu-modified CeO_2 via redox-coupled atomic layer deposition for CO oxidation, Nat. Commun., 11 (2020) 4240.

79. Jiang, D.; Wan, G.; Garcia-Vargas, C.E.; Li, L.Z.; Pereira-Hernandez, X.I.; Wang, C.M.; Wang, Y., Elucidation of the Active Sites in Single-Atom Pd_1/CeO_2 Catalysts for Low-Temperature CO Oxidation, ACS Catal., 10 (2020) 11356-11364.

80. Cha, B.J.; Kim, S.Y.; Choi, C.M.; Sung, J.Y.; Choi, M.C.; Seo, H.O.; Kim, Y.D., Ultra-low loading of iron oxide on Pt/Al_2O_3 for enhanced catalytic activity of CO oxidation at room temperature: A simple method for applications, Chem. Eng. J., 404 (2021) 126560.

81. Bera, P.; Hegde, M.S., Recent advances in auto exhaust catalysis, J. Indian Inst. Sci., 90 (2010) 299-325.

82. Zhao, D.Y.; Feng, J.L.; Huo, Q.S.; Melosh, N.; Fredrickson, G.H.; Chmelka, B.F.; Stucky, G.D., Triblock Copolymer Syntheses of Mesoporous Silica with Periodic 50 to 300 Angstrom Pores, Science, 279 (1998) 548-552.

83. Delannoy, L.; El Hassan, N.; Musi, A.; Le To, N.N.; Krafft, J.-M.; Louis, C., Preparation of Supported Gold Nanoparticles by a Modified Incipient Wetness Impregnation Method, J. Phys. Chem. B, 110 (2006) 22471-22478.

84. Chang, F.-W.; Kuo, M.-S.; Tsay, M.-T.; Hsieh, M.-C., Hydrogenation of CO_2 over nickel catalysts on rice husk ash-alumina prepared by incipient wetness impregnation, Appl. Catal. A: Gen., 247 (2003) 309-320.

85. Packer, A.P.; Larivière, D.; Li, C.; Chen, M.; Fawcett, A.; Nielsen, K.; Mattson, K.; Chatt, A.; Scriver, C.; Erhardt, L.S., Validation of an inductively coupled plasma mass spectrometry (ICP-MS) method for the determination of cerium, strontium, and titanium in ceramic materials used in radiological dispersal devices (RDDs), Anal. Chim. Acta, 588 (2007) 166-172.

86. Klug, H.P.; Alexander, L.E. *X-Ray Diffraction Procedures: For Polycrystalline and Amorphous Materials*; John Wiley & Sons: London (UK), **1962**.

87. Tarazona, P., Free-Energy Density Functional for Hard-Spheres, Phys. Rev. A, 31 (1985) 2672-2679.

88. Tarazona, P.; Marconi, U.M.B.; Evans, R., Phase equilibria of fluid interfaces and confined fluids: Non-local versus local density functionals, Molec. Phys., 60 (1987) 573-595.

89. Cara, C.; Rombi, E.; Musinu, A.; Mameli, V.; Ardu, A.; Sanna Angotzi, M.; Atzori, L.; Niznansky, D.; Xin, H.L.; Cannas, C., MCM-41 support for ultrasmall g-Fe_2O_3 nanoparticles for H_2S removal, J. Mater. Chem. A, 5 (2017) 21688-21698.

90. Meloni, D.; Monaci, R.; Zedde, Z.; Cutrufello, M.G.; Fiorilli, S.; Ferino, I., Transesterification of soybean oil on guanidine base-functionalized SBA-15 catalysts, Appl. Catal. B: Environ., 102 (2011) 505-514.

91. Jiménez-Gómez, C.P.; Cecilia, J.A.; Alba-Rubio, A.C.; Cassidy, A.; Moreno-Tost, R.; García-Sancho, C.; Maireles-Torres, P., Tailoring the selectivity of Cu-based catalysts in the furfural hydrogenation reaction: Influence of the morphology of the silica support, Fuel, 319 (2022) 123827.

92. Rouquerol, F.; Rouquerol, J.; Sing, K.S.W.; Llewellyn, P.; Maurin, G. Adsorption by Powders and Porous Solids: Principles, Methodology and Applications - 2nd edition. Elsevier: Amsterdam (NL), **2014**; pp. 12-13.

93. Hou, X.Y.; Qian, J.N.; Li, L.L.; Wan, F.; Li, B.; He, F.L.; Fan, M.G.; Tong, Z.F.; Dong, L.H.; Dong, L., Preparation and Investigation of Iron-Cerium Oxide Compounds for NO_x Reduction, Ind. Eng. Chem. Res., 57 (2018) 16675-16683.

94. Lykaki, M.; Stefa, S.; Carabineiro, S.A.C.; Pandis, P.K.; Stathopoulos, V.N.; Konsolakis, M., Facet-Dependent Reactivity of Fe_2O_3/CeO_2 Nanocomposites: Effect of Ceria Morphology on CO Oxidation, Catalysts, 9 (2019) 371.

95. Danielis, M.; Betancourt, L.E.; Orozco, I.; Divins, N.J.; Llorca, J.; Rodríguez, J.A.; Senanayake, S.D.; Colussi, S.; Trovarelli, A., Methane oxidation activity and nanoscale characterization of Pd/CeO_2 catalysts prepared by dry milling Pd acetate and ceria, Appl. Catal. B: Environ., 282 (2021) 119567.

96. Khan, S.B.; Faisal, M.; Rahman, M.M.; Jamal, A., Exploration of CeO_2 nanoparticles as a chemi-sensor and photo-catalyst for environmental applications, Sci. Total Environ., 409 (2011) 2987-2992.

97. Jie, W.; Liu, Y.; Deng, W.; Liu, Q.; Qiu, M.; Liu, S.; Hu, J.; Gong, L., Effect of one-dimensional ceria morphology on CuO/CeO_2 catalysts for CO preferential oxidation, J. Solid State Chem., 311 (2022) 123109.

98. Pu, Z.-Y.; Liu, X.-S.; Jia, A.-P.; Xie, Y.-L.; Lu, J.-Q.; Luo, M.-F., Enhanced Activity for CO Oxidation over Pr- and Cu-Doped CeO_2 Catalysts: Effect of Oxygen Vacancies, J. Phys. Chem. C, 112 (2008) 15045-15051.

99. Hadjiivanov, K.I.; Vayssilov, G.N. Characterization of oxide surfaces and zeolites by carbon monoxide as an IR probe molecule. In *Advances in Catalysis*, Gates, B.C., Knozinger, H., Eds.; Elsevier Academic Press Inc: San Diego, **2002**; Volume 47, pp. 307-511.

100. Rojas-Buzo, S.; Concepción, P.; Olloqui-Sariego, J.L.; Moliner, M.; Corma, A., Metalloenzyme-Inspired Ce-MOF Catalyst for Oxidative Halogenation Reactions, ACS Appl. Mater. Interfaces, 13 (2021) 31021-31030.

101. Chavan, S.; Bonino, F.; Vitillo, J.G.; Groppo, E.; Lamberti, C.; Dietzel, P.D.C.; Zecchina, A.; Bordiga, S., Response of CPO-27-Ni towards CO, N_2 and C_2H_4, Phys. Chem. Chem. Phys., 11 (2009) 9811-9822.

102. Komurcu, M.; Lazzarini, A.; Kaur, G.; Borfecchia, E.; Oien-Odegaard, S.; Gianolio, D.; Bordiga, S.; Lillerud, K.P.; Olsbye, U., Co-catalyst free ethene dimerization over Zr-based metal-organic framework (UiO-67) functionalized with Ni and bipyridine, Catal. Today, 369 (2021) 193-202.

103. Sadykov, V.A.; Simonov, M.N.; Mezentseva, N.V.; Pavlova, S.N.; Fedorova, Y.E.; Bobin, A.S.; Bespalko, Y.N.; Ishchenko, A.V.; Krieger, T.A.; Glazneva, T.S.; Larina, T.V.; Cherepanova, S.V.; Kaichev, V.V.; Saraev, A.A.; Chesalov, Y.A.; Shmakov, A.N.; Roger, A.C.; Adamski, A., Ni-loaded nanocrystalline ceria-zirconia solid solutions prepared via modified Pechini route as stable to coking catalysts of CH_4 dry reforming, Open Chem., 14 (2016) 363-376.

104. Binet, C.; Daturi, M.; Lavalley, J.C., IR study of polycrystalline ceria properties in oxidised and reduced states, Catal. Today, 50 (1999) 207-225.

105. Bozon-Verduraz, F.; Bensalem, A., IR studies of cerium dioxide: influence of impurities and defects J. Chem. Soc. Faraday Trans., 90 (1994) 653-657.

106. Ivanova, E.; Mihaylov, M.; Hadjiivanov, K.; Blasin-Aube, V.; Marie, O.; Plesniar, A.; Daturi, M., Evidencing three distinct Fe^{II} sites in Fe-FER zeolites by using CO and NO as complementary IR probes, Appl. Catal. B: Environ., 93 (2010) 325-338.

107. Mihaylov, M.; Ivanova, E.; Drenchev, N.; Hadjiivanov, K., Coordination Chemistry of Fe^{2+} Ions in Fe,H-ZSM-5 Zeolite as Revealed by the IR Spectra of Adsorbed CO and NO, J. Phys. Chem. C, 114 (2010) 1004-1014.

108. Szanyi, J.; Gao, F.; Kwak, J.H.; Kollar, M.; Wang, Y.L.; Peden, C.H.F., Characterization of Fe^{2+} ions in Fe,H/SSZ-13 zeolites: FTIR spectroscopy of CO and NO probe molecules, Phys. Chem. Chem. Phys., 18 (2016) 10473-10485.

109. Kim, G.; Shin, S.; Choi, Y.; Kim, J.; Kim, G.; Kim, K.-J.; Lee, H., Gas-Permeable Iron-Doped Ceria Shell on Rh Nanoparticles with High Activity and Durability, JACS Au, 2 (2022) 1115-1122.

110. Tumuluri, U.; Rother, G.; Wu, Z.L., Fundamental Understanding of the Interaction of Acid Gases with CeO_2: From Surface Science to Practical Catalysis, Ind. Eng. Chem. Res., 55 (2016) 3909-3919.

111. Yu, Y.B.; Takei, T.; Ohashi, H.; He, H.; Zhang, X.L.; Haruta, M., Pretreatments of Co_3O_4 at moderate temperature for CO oxidation at -80 ℃, J. Catal., 267 (2009) 121-128.

112. Zhang, W.J.; PalDey, S.; Deevi, S., Effect of moisture on the active species in Cu-CeO_2 catalyst, Appl. Catal. A: Gen., 295 (2005) 201-208.